nature communications

Article

https://doi.org/10.1038/s41467-024-55116-x

Steering acidic oxygen reduction selectivity of single-atom catalysts through the second sphere effect

Received: 2 June 2024

Accepted: 2 December 2024

Published online: 30 December 2024

Check for updates

Haiyuan Zou[1,11], Siyan Shu[1,2,11], Wenqiang Yang[3,11], You-chiuan Chu[4], Minglun Cheng[5], Hongliang Dong[6], Hong Liu[1], Fan Li[1], Junhui Hu[1], Zhenbin Wang[3,7], Wei Liu[8], Hao Ming Chen[4] & Lele Duan[2,9,10]

Natural enzymes feature distinctive second spheres near their active sites, leading to exquisite catalytic reactivity. However, incumbent synthetic strategies offer limited versatility in functionalizing the second spheres of heterogeneous catalysts. Here, we prepare an enzyme-mimetic single Co–N_4 atom catalyst with an elaborately configured pendant amine group in the second sphere via 1,3-dipolar cycloaddition, which switches the oxygen reduction reaction selectivity from the $4e^-$ to the $2e^-$ pathway under acidic conditions. Proton inventory studies and theoretical calculations reveal that the introduced pendant amine acts as a proton relay and promotes the protonation of $*O_2$ to *OOH on the Co–N_4 active site, facilitating H_2O_2 production. The second sphere-tailored Co–N_4 sites reach optima H_2O_2 selectivity of 97% ± 1.13%, showing a 3.46-fold enhancement to bare Co–N_4 catalyst (28% ± 1.75%). This work provides an appealed approach for enzyme-like catalyst design, bridging the gap between enzymatic and heterogeneous catalysis.

Metallo-oxidase enzymes display extraordinary oxygen reduction reactivities by optimizing the microenvironment around their active centers[1,2]. Studies of the active sites of heme-based cytochrome c oxidase or copper-based multicopper oxidases have revealed that the second sphere effects, especially hydrogen bonding (Fig. 1a), manipulate the O_2 activation and stabilize/activate the hydroperoxido ligand[3–5]. However, metallo-oxidases are often prone to degradation outside of their native cell environments and have a low density of active sites, leading to a long-standing challenge – the demand for developing synthetic catalysts that mimic the characteristics of the active sites of oxidases. Although advancements in synthetic techniques provide nearly limitless possibilities for manipulating the second sphere of homogeneous oxygen reduction catalysts, the regulation of the second sphere for heterogeneous oxygen reduction catalysts remains constrained[6,7]. A few reports on the second coordination sphere regulation of heterogeneous oxygen reduction catalysts via heteroatom doping are based on the induction effect, instead of the second sphere effects, of induced heteroatoms.

Single-atom catalysts (SACs) with discrete metal centers embedded on the substrate have emerged as potent catalysts for extensive electrochemical applications by virtue of their high atom utilization and unsaturated coordination sphere[8,9]. Integrating a second sphere

[1]Department of Chemistry, Southern University of Science and Technology, Shenzhen, China. [2]Center of Artificial Photosynthesis for Solar Fuels and Department of Chemistry, School of Science, Westlake University, Hangzhou, China. [3]Catalysis Theory Center, Department of Physics, Technical University of Denmark, Lyngby, Denmark. [4]Department of Chemistry and Center for Emerging Materials and Advanced Devices, National Taiwan University, Taipei, Taiwan. [5]Hebei Key Laboratory of Active Components and Functions in Natural Products, College of Chemical Engineering, Hebei Normal University of Science and Technology, Qinhuangdao, China. [6]Center for High Pressure Science and Technology Advanced Research, Shanghai, China. [7]Department of Materials Science and Engineering, City University of Hong Kong, Hong Kong, SAR, China. [8]School of Chemistry, Dalian University of Technology, Dalian, China. [9]Division of Solar Energy Conversion and Catalysis at Westlake University, Zhejiang Baima Lake Laboratory Co. Ltd, Hangzhou, Zhejiang, China. [10]Institute of Natural Sciences, Westlake Institute for Advanced Study, Hangzhou, China. [11]These authors contributed equally: Haiyuan Zou, Siyan Shu, Wenqiang Yang. e-mail: duanlele@westlake.edu.cn

https://doi.org/10.1038/s41467-024-55116-x

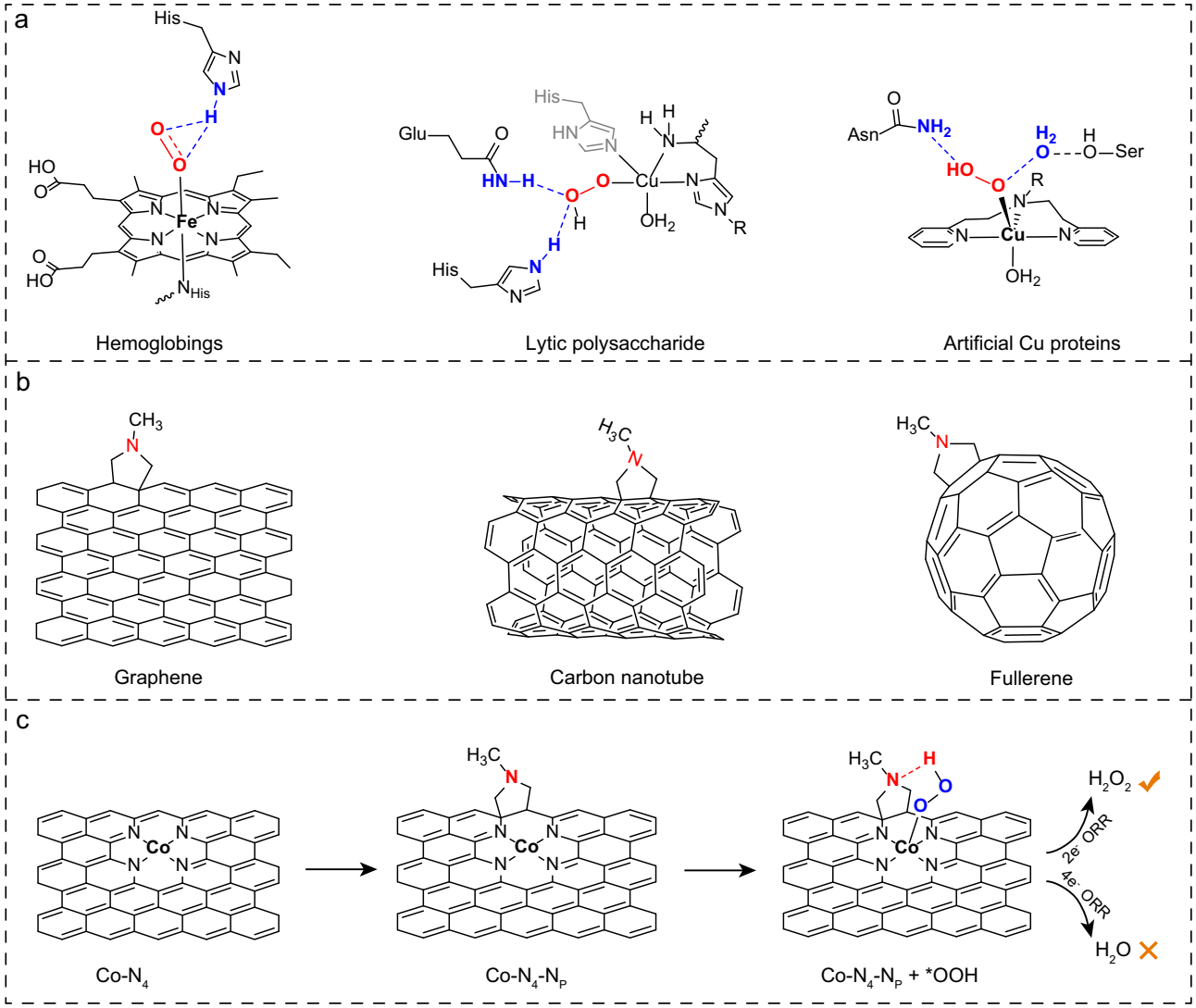

Fig. 1 | Scheme illustrations. a Representations of the hydrogen bonds involved in stabilizing the Fe-O_2 species of the active sites of hemoglobins, the Cu-OOH intermediate of Cu-dependent lytic polysaccharide monooxygenases, and the Cu-OOH species of artificial Cu proteins. **b** Functionalization of graphene, carbon nanotube and fullerene with the N_P group by the 1,3-dipolar cycloaddition reaction. **c** Schematic illustration of the construction of the N_P second sphere on Co-N_4 and the second sphere effect in stabilizing the *OOH intermediate toward 2e$^-$ ORR pathway.

proximal to metal centers of SACs, for instance, M–N_4 SACs, may resemble the structure-dependent catalytic properties of a metalloenzyme[10]. A daunting challenge in designing such enzyme-like SACs catalysts requires the precise configuration of functional groups in the second sphere[11]. Taking the widely-document single metal atoms on the carbonaceous backbone as a representative example, the typically M–N_4 moieties are usually derived by the pyrolysis process at high temperatures, which is hard to secure the second sphere[12–14]. A common way to vary the M–N_4 local environment is achieved via heteroatom (e.g., S, O, P) doping while the structure of the active site is often changed in an uncontrolled fashion, far behind the level of atomic precision[15–18].

Surface covalent chemistry offers versatile platforms for grafting functional groups on carbonaceous material[19]. It has been witnessed that the surface-functionalized carbonaceous (e,g., graphene, carbon nanotube, fullerene) with a five-membered ring could be readily prepared via the cycloaddition between a 1,3-dipole and the dipolarophile (carbon) (Fig. 1b)[20–23]. Nonetheless, the 1,3-dipolar cycloaddition on carbon-supported SACs catalysts, to the best of our knowledge, has not been documented yet. Given that the LUMO of the electron-deficient dipolarophile normally favors interaction with the HOMO of the dipole[24], the positively polarized carbon atoms around the M–N_4 site shall be more reactive to the 1,3-dipole. Thus, covalent chemistry through 1,3-dipolar cycloaddition is expected to establish the second sphere around the M–N_4 sites, mimicking the local environments of enzymes.

We report herein that a second sphere of pendant amine (referred to N_P henceforth) is configured near the Co–N_4 site using the 1,3-dipolar cycloaddition reaction (Fig. 1c). The introduced N_P second sphere demonstrates the structure-dependent property of metalloenzyme in a proof-of-concept demonstration for the acidic electrochemical oxygen reduction reaction (ORR), substantially altering the O_2 reduction pathway from 4e$^-$-ORR on Co-N_4 to 2e$^-$-ORR on Co-N_4-N_P (see their chemical structures in Fig. 1c). Proton inventory study and theoretical simulation gain insight that the N_P second sphere acts as a proton relay, facilitating O_2 protonation and stabilizing the *OOH intermediate on Co–N_4 centers, thereby steering the ORR from the 4e$^-$-path to the 2e$^-$-path. Consequently, the hydrogen peroxide selectivity of Co-N_4-N_P shows a 3.46-fold enhancement compared with Co-N_4, improving from 28% ± 1.75 to 97% ± 1.13%. The present study highlights a bio-inspired second sphere interaction for fine-tuned catalytic properties, providing a representative platform for the rational design of enzyme-like catalysts across myriad catalytic applications.

https://doi.org/10.1038/s41467-024-55116-x

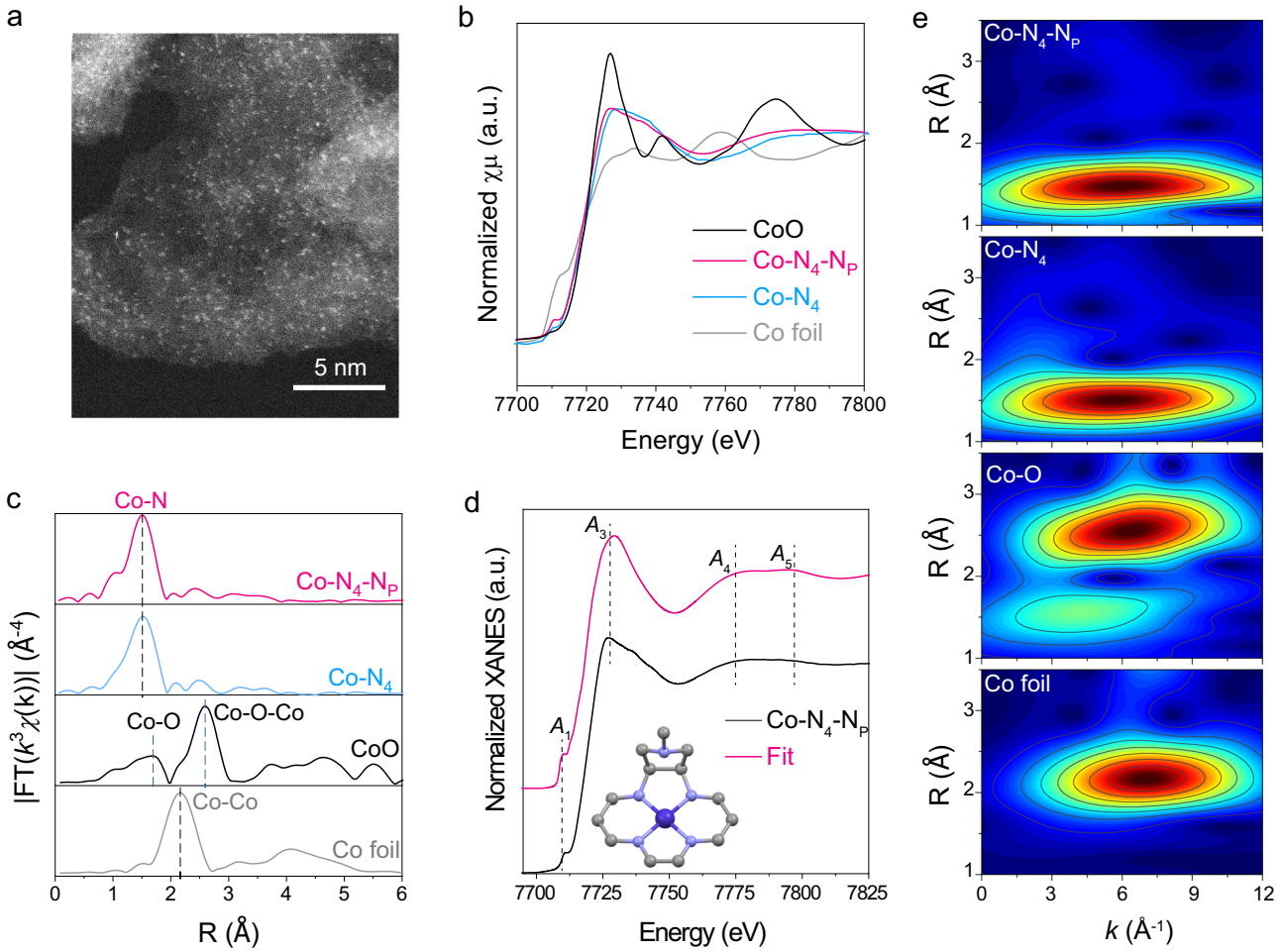

Fig. 2 | Morphological and structural characterizations. a HAADF-STEM image of Co-N_4-N_P. **b** Co *K*-edge XANES and **c** FT-EXAFS spectra of Co-N_4, Co-N_4-N_P and reference samples. **d** Comparison between the experimental XANES spectrum and theoretical one calculated with the depicted structures of Co-N_4-N_P. (insert is the correlative atomic structures). **e** Co *K*-edge WT-EXAFS contour plots for Co-N_4, Co-N_4-N_P and reference samples.

Results

Material synthesis and characterization

We leverage the prevalent Co-N_4/graphene as a prototype to elucidate how the second sphere substituents near the Co active sites profoundly affect the ORR performance. First, a metal-free N-dope carbon substrate (NC) and an NC-supported single-atom Co catalyst (Co-N_4, Methods) were synthesized according to the known procedure[25]. Next, the facile 1,3-dipolar cycloaddition of an azomethine ylide with Co-N_4 was carried out to covalently graft the $-CH_2NMeCH_2-$ bridge with a pendant amine group (N_p) on Co-N_4 using sarcosine and paraformaldehyde as dipole precursors, and the resulting material was denoted as Co-N_4-N_p (Supplementary Fig. 1). Besides, the N_p functionalized NC (NC-N_p) was also prepared in the same way. The loading amount of Co on Co-N_4 and Co-N_4-N_P was calculated to be 1.2 wt% by inductively coupled plasma mass spectrometry (ICP-MS). The as-synthesized materials display a nanoflake-like morphology with flake sizes around 5–10 nm (Supplementary Fig. 2b). The high-resolution transmission electron microscopy (TEM) images show onion-like lattice stripes without notable nanoparticles (Supplementary Fig. 2c). The Co-N_4-N_P inherits the morphology of its parent Co-N_4, and no metal aggregation was detected, suggesting that the 1,3-dipolar cycloaddition process did not destroy the pristine material texture (Supplementary Figs. 3b and 3c). The absence of metal nanoparticles is also reflected by their X-ray diffraction patterns (XRD), where two broad peaks at 23° and 43° are associated with diffraction from the 002 and 100/101 set of planes of the carbon materials (Supplementary Fig. 4a)[26]. For their Raman spectra (Supplementary Fig. 4b), the characteristic *D* and *G* bands are at 1356 cm^{-1} and 1540 cm^{-1}, respectively. To get a close view of the atomic dispersion of Co sites, the aberration-corrected high-angle annular dark-field scanning TEM (HAADF-STEM) was recorded. As illustrated in Fig. 2a and Supplementary Figs. 2d, 2e, 3d, 3e, isolated bright dots of single Co sites are homogeneously dispersed on the carbon matrix for both Co-N_4 and Co-N_4-N_P samples. X-ray energy dispersive spectroscopic (EDS)-mapping images also present uniformly distributed C, N, and Co elements across the material (Supplementary Figs. 2f–2i and 3f–3i).

Synchrotron-based X-ray absorption near-edge structure (XANES) and extended X-ray absorption fine structure (EXAFS) analysis were conducted to gain the local physicochemical information of Co sites. From the XANES profiles, the near-edge position of the Co *K*-edge of both Co-N_4 and Co-N_4-N_P was situated between Co foil and CoO, suggesting the oxidation state of the as-prepared Co single-atoms between 0 and +2 (Fig. 2b). Close inspection showed that Co-N_4-N_P exhibited damped shoulder peak at 7716 eV, which corresponds to $1s \rightarrow 4p_z$ transition, in comparison to Co-N_4 counterpart. This observation is to a large extent correlated with the disruption of in-plane symmetry. The core-level X-ray photoelectron spectra of Co 2*p* further suggest the partially oxidized Co sites due to the electron transfer from Co to the substrate (Supplementary Fig. 5). Noteworthy, no energy shift occurred in Co *K*-edge and Co 2*p* spectra between Co-N_4 and Co-N_4-N_P, revealing that the decorating $-CH_2NMeCH_2-$ group introduced by 1,3-dipolar cycloaddition does not change the electronic

https://doi.org/10.1038/s41467-024-55116-x

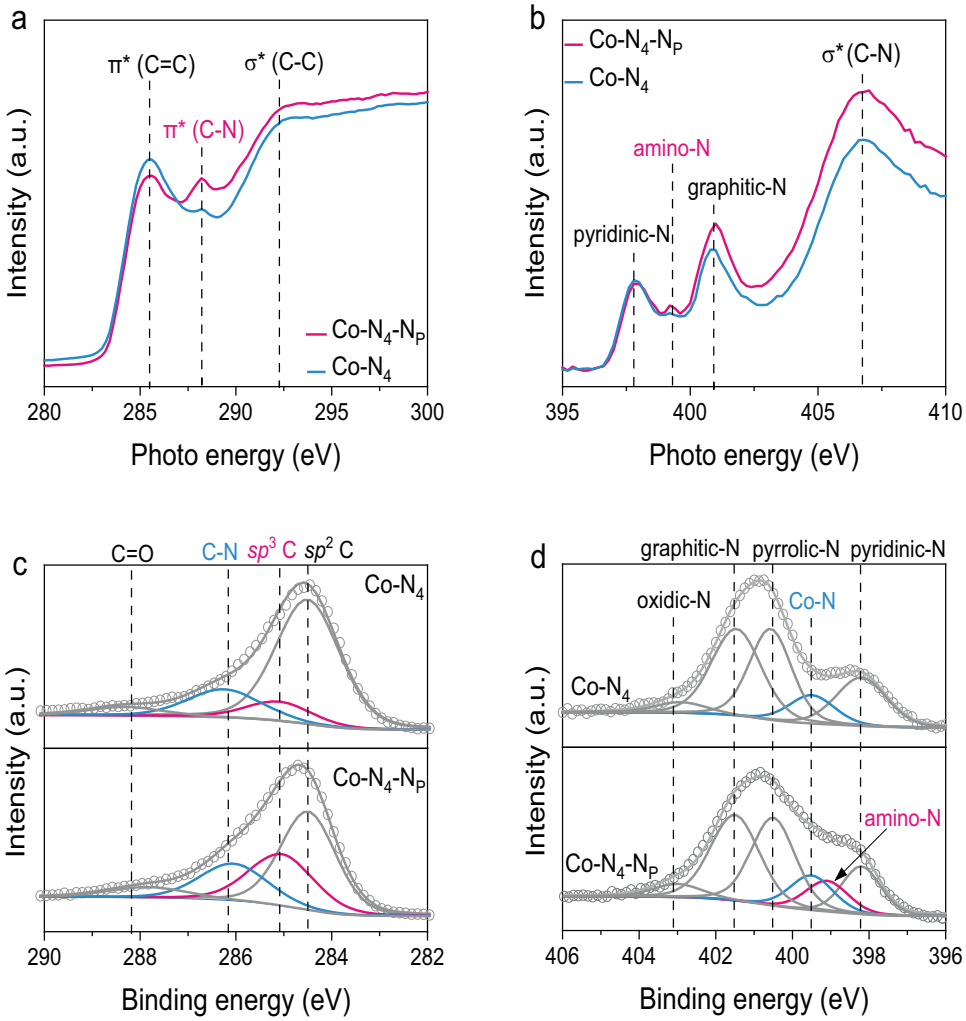

Fig. 3 | XANES and XPS spectra. Soft XANES spectra of **a** C *K*-edge and **b** N *K*-edge of Co-N_4 and Co-N_4-N_P. **c** C 1*s* and **d** N 1*s* XPS spectra of Co-N_4 and Co-N_4-N_P.

state of Co sites (Supplementary Fig. 6-lower). The local structural information of Co can be further identified by the EXAFS analysis. The Fourier-transformed (FT) k^3-weighted EXAFS profiles of Co-N_4 and Co-N_4-N_P at Co *K*-edge present a prominent peak at approximately 1.45 Å, while the presence of Co–Co bonds in higher *R*-regions is negligible, signifying the single atomic feature was well-crafted (Fig. 2c). Furthermore, additional evidence of wavelet transform (WT) analysis extracted from the EXAFS oscillations in *R*- and *k*-spaces was conducted to validate the localized coordination configuration of Co single atoms. As shown in Fig. 2e, both Co-N_4 and Co-N_4-N_P present a WT intensity maximum at 5.5 $Å^{-1}$, but the absence of the intensity maximum of Co–Co (6.6 $Å^{-1}$) at the first shell, corroborating the atomic distributed Co sites in the N-doped carbon substrate. The EXAFS fitting results for the first shell show that the average coordination number of Co is approximately 4, implying the atomic Co–N_4 moieties embedded in the Co-N_4-N_P (Supplementary Fig. 7 and Supplementary Table 1). Based on the structural information explored, it can be inferred that the grafted amine group is presumably positioned in proximity to the Co-N_4 center (Fig. 2d and Supplementary Fig. 9). Building upon the following characterization and experiments, the most appropriate structural model of Co-N_4-N_P is established (inset Fig. 2d), but the concrete position of the pendant amine is still limited by the resolution of current techniques, which will require further techniques for confirmation.

To identify the functional group grafted on Co-N_4, Fourier transform infrared spectroscopy (FTIR) was employed. In Supplementary Fig. 10, the Co-N_4-N_P exclusively renders fingerprint vibration bands at 1260 cm^{-1}, 1402 cm^{-1}, 2780 cm^{-1} and 2815 cm^{-1}, which are ascribed to the C–N stretching vibration and C–H bending/stretching vibration of the $-CH_2NMeCH_2-$ group, respectively[27]. Furthermore, soft XANES and X-ray photoelectron spectroscopy (XPS) were carried out to scrutinize the local electronic states of C and N in Co-N_4 and Co-N_4-N_P. As shown in Fig. 3a, the normalized C *K*-edge XANES spectra present unoccupied π* and excited σ* states. The peaks centered at 285.4 eV and 287.2 eV are attributed to the 1*s*–π* from sp^2 C=C and the π* excitation in charge transfer between C and N in the C–N bond, respectively[28,29]. Interestingly, the Co-N_4-N_P exhibits a decreased π* (C=C) and increased π* (C–N) intensity than that of the original Co-N_4, which is reasoned by introducing sp^3-C and C–N species as a consequence of N_P modulation. Moreover, the enhancement of the relative ratio of sp^3-C and C–N species can also be discovered on the C 1*s* core-level of Co-N_4-N_P compared to the Co-N_4, echoing the XANES results (Fig. 3b). Furthermore, from the N *K*-edge XANES spectra, three distinct peaks at 397.8, 400.9 and 406.7 eV, respectively, assigned to the pyridinic-N, graphitic-N and σ*(C–N) species[30,31], are observed on both Co-N_4 and Co-N_4-N_P. Of note, an additional peak centered at 399.2 eV, giving rise to amino-N[32], was exclusively observed on the Co-N_4-N_P (Fig. 3c). The deconvolution of N 1*s* XPS spectra also verified the presence of amino-N in Co-N_4-N_P at a peak position of 399.2 eV[33]. The other five peaks at 398.2, 399.6, 400.6, 401.5 and 403.1 eV are associated with the pyridinic-N, Co-N, pyrrolic-N, graphitic-N and oxidized-N, respectively. The N content at the surface of Co-N_4 and Co-N_4-N_P are

https://doi.org/10.1038/s41467-024-55116-x

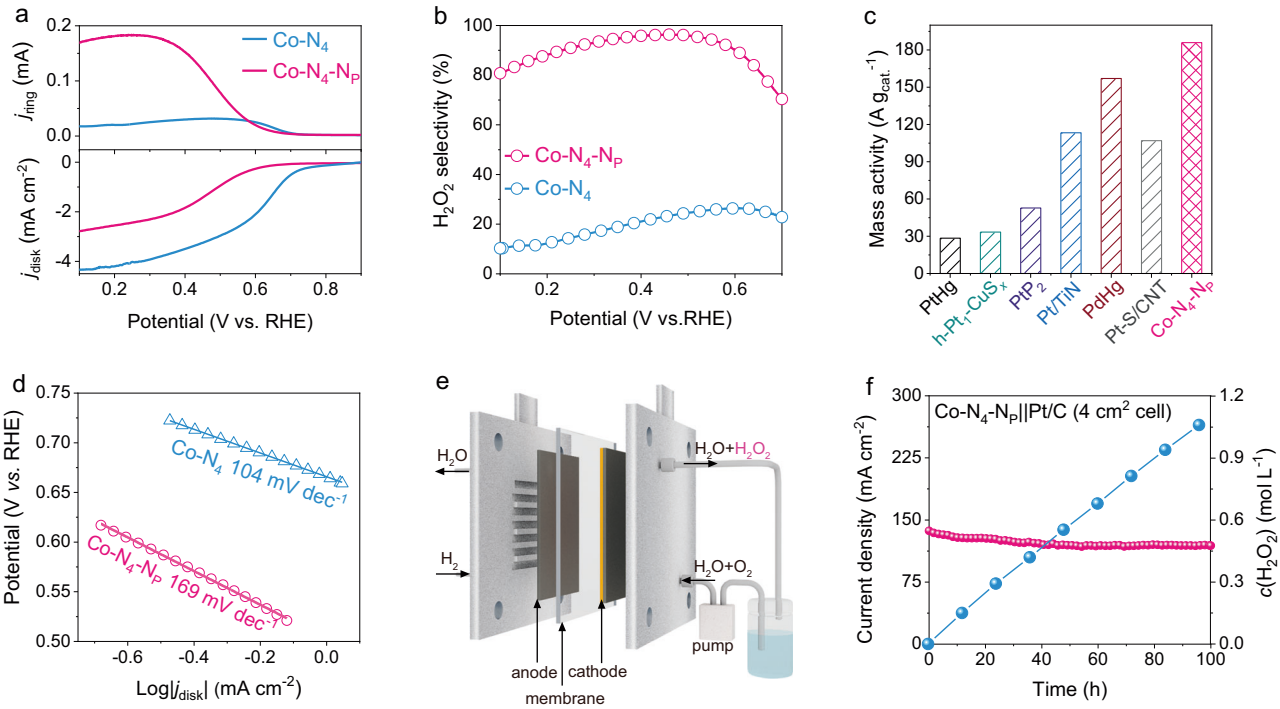

Fig. 4 | ORR performance of Co-N_4 and Co-N_4-N_P. a The polarization curves of disk current density and ring current in 0.10 M $HClO_4$ with iR correction at 1600 rpm. **b** The calculated H_2O_2 selectivity as a function of the applied potential. **c** Mass activity comparison at 0.5 V vs. RHE for Co-N_4-N_P and previously reported catalysts. **d** The corresponding Tafel plots. **e** Schematic illustration of MEA for H_2O_2 electroproduction. **f** Chronoamperometry stability tests of Co-N_4-N_P at 0.6 V for 100 h.

5.2 at% and 7.6 at%, respectively. The enhancement of N content for Co-N_4-N_P was ascribed to the additional amino-N species (Fig. 3d). In the same vein, the characteristic amino-N was also observed in the metal-free NC-N_P, which suggests the well-grafted N_P group (Supplementary Fig. 11). To further confirm the assignment of N 1*s* and sp^3-C 1*s* peaks of the N_p group, 1,3-dipolar cycloaddition was carried out on the commercial graphene sheets without any N element, and the functionalized graphene is named as G-N_p[20,21]. As expected, the N element with content of ~2.2 at% was evenly distributed across G-N_p after surface modulation (Supplementary Fig. 12). The amino-N and sp^3-C intensity (Supplementary Fig. 13) were enriched on G-N_p, which confirmed the powerful covalent functionalization of the 1,3-dipolar cycloaddition reaction. Overall, these finding sufficiently underscores the successful surface functionalization with the pendant amine group.

Electrochemical ORR tests

The ORR can undergo either a $4e^-$ or $2e^-$ reduction pathway, the selectivity of which is scaled by the propensity of the O–O bond cleavage over the catalysts. As mentioned above, metalloenzymes utilize the hydrogen bonding in the second sphere to manipulate the O–O bond cleavage. We thereby conducted the ORR experiments to investigate the second sphere effect of N_P on the ORR. As such, the ORR performance was examined in an oxygen-saturated 0.10 M $HClO_4$ aqueous electrolyte using a rotating ring-disk electrode at 1600 r.p.m. The amount of H_2O_2 yield was evaluated by the Pt-ring electrode, which was held at 1.20 V versus the reversible hydrogen electrode (vs. RHE) to guarantee only H_2O_2 oxidization. Figure 4a presents the polarization curves of Co-N_4 and Co-N_4-N_P, where distinct ORR performances are derived. The Co-N_4, composed of Co–N_4 active sites, contributes a fast ORR response with an onset potential of 0.82 V. The corresponding diffusion limiting current density (j_L) was achieved as high as 4.21 mA cm^{-2}, and the ring current is humble (0.032 mA). Therefore, a moderate H_2O_2 selectivity of 28% ± 1.75% along with an electron transfer number (n) of 3.51–3.83 was delivered, rendering a typical $4e^-$ ORR pathway over Co-N_4 (Fig. 4b and Supplementary Fig. 14). In stark contrast, the Co-N_4-N_P exhibited a decreased onset potential of 0.63 V vs. RHE (closer to the thermodynamic limit of $2e^-$ ORR at 0.70 V) and a low j_L value compared to the Co-N_4. Of note, the ring current density was dramatically promoted to 0.185 mA at 0.30 V *vs.* RHE, five times higher than that of Co-N_4 (Fig. 4a). Accordingly, an optimum H_2O_2 selectivity of 97% ± 1.13% and Faraday efficiency of 91% ± 1.13% were achieved for the Co-N_4-N_P, which is 3.46 folds as high as that of Co-N_4 (Fig. 4b and Supplementary Fig. 15), suggesting distinctive ORR routes caused by the second sphere perturbation. Of note, the mass activity of Co-N_4-N_P (186.20 A $g_{cat.}^{-1}$) at 0.5 V vs. RHE is even better than many noble-metal catalysts, such as PtHg (28.42 A $g_{cat.}^{-1}$)[34], h-Pt_1-CuS_x (33.40 A $g_{cat.}^{-1}$)[35], PtP_2 (52.80 A $g_{cat.}^{-1}$)[36], Pt/TiN (113.30 A $g_{cat.}^{-1}$)[37], Pt-S/CNT (107.10 A $g_{cat.}^{-1}$)[38], and PdHg (157.40 A $g_{cat.}^{-1}$)[39] (Fig. 4c). Such high H_2O_2 selectivity and mass activity make Co-N_4-N_P a superior ORR catalyst for H_2O_2 electroproduction under acidic conditions.

The electron transfer number over the Co-N_4-N_P is calculated to be 2.07–2.60, suggesting a preferential $2e^-$ ORR route (Supplementary Fig. 14). Tafel slope analysis also reflected a shifted ORR kinetic between Co-N_4-N_P (169 mV dec^{-1}) and Co-N_4 (104 mV dec^{-1}) (Fig. 4d). The TOF of the Co-N_4-N_P for H_2O_2 formation was estimated to be 0.23 ± 0.03 s^{-1} and 0.45 ± 0.05 s^{-1} at 0.50 V and 0.40 V vs. RHE, respectively, much higher than that of Co-N_4 (Supplementary Fig. 16). Control experiments using metal-free NC and NC-N_P show poor ORR activity, signifying that the functionalized N_P group does not, on its own, contribute notably to the H_2O_2 production (Supplementary Fig. 17). Accordingly, it is the second sphere rather than the change of the intrinsic electronic structure of Co-N_4 that steers the ORR selectivity, which is essentially different to the recent studies on the first coordination sphere regulation[40–42]. The durability of Co-N_4-N_P was evaluated on RRDE at a disk potential of 0.50 V. As shown in Supplementary Fig. 18, insignificant current declination was observed with a stable H_2O_2 selectivity above 85% under 10 h continuous operation. The time-dependent morphology of Co-N_4-N_P were examined using in situ electrochemical TEM (Supplementary Fig. 19). Analysis depicted in

https://doi.org/10.1038/s41467-024-55116-x

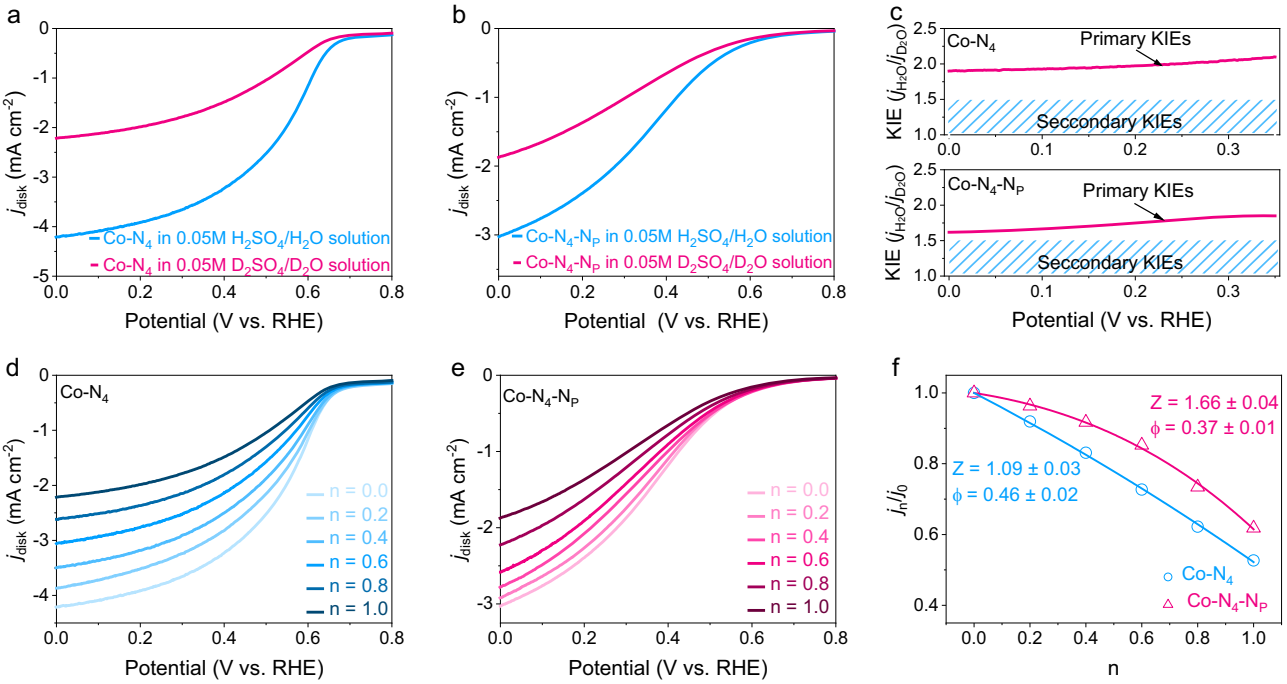

Fig. 5 | Kinetic isotope effects and proton inventory studies. LSV curves of **a** Co-N_4 and **b** Co-N_4-N_P in aqueous 0.050 M H_2SO_4 solutions and 0.050 M D_2SO_4/D_2O solutions with iR correction at 1600 rpm. **c** The corresponding kinetic isotope effect against potential. LSV curves of **d** Co-N_4 and **e** Co-N_4-N_P in mixed solutions of 0.050 M H_2SO_4/H_2O and 0.050 M D_2SO_4/D_2O with different ratios (n indicates the atom fraction of deuterium of the given solution). **f** The plots of j_n/j_0 against n, where n = [D]/([D] + [H]).

Supplementary Fig. 20 and Fig. 21 revealed no discernible changes in morphology or detectable crystal diffraction over 40 min of electrolysis, thus ruling out the aggregation of Co particles formed during the ORR process. Furthermore, operando XAS measurements were conducted to evaluate the structural stability of Co-N_4-N_P during the ORR process (Supplementary Fig. 22c). As shown in Supplementary Fig. 22a, the Co *K*-edge XANES profiles of Co-N_4-N_P at different electrolysis times closely resemble those of the dry Co-N_4-N_P powder and Co-N_4-N_P under open circuit conditions, with pronounced pre-edge features throughout the electrolysis process. Additionally, the FT k^3-weighted EXAFS profiles of Co-N_4-N_P display a prominent peak at 1.45 Å, with no observable peaks for Co-Co coordination during the ORR measurement Supplementary Fig. 22b). Post-stability test analysis in Supplementary Fig. 23 further confirms the well-maintained single-atom morphology and chemical composition of Co-N_4-N_P. These results affirm the structural and electrochemical robustness of Co-N_4-N_P during the ORR process.

By taking advantage of the superior 2e$^-$ ORR reactivity of Co-N_4-N_P, we have fabricated a membrane electrode assembly (MEA) for the direct electrosynthesis of pure aqueous H_2O_2 solutions (Supplementary Fig. 24). As illustrated in Fig. 4e, the MEA was fabricated by sandwiching cathode (Co-N_4-N_P) and anode (Pt/C) layers with a Nafion exchange membrane. A mixture of O_2 and liquid H_2O was continuously fed in the cathode chamber, and a humidified H_2 gas stream flowed over the anode. In principle, HO_2^- ions generated by the ORR on Co-N_4-N_P quickly interacted with H^+ derived by the hydrogen oxidation reaction on the Pt/C anode, forming the H_2O_2 product. From the current-voltage curve, a current density of 29.39 mA cm^{-2} was achieved at 0.00 V, signifying the favorable H_2O_2 production without the expense of the external energy input (Supplementary Fig. 25). Over a wide cell potential window from 0.00 V to 1.00 V, a high H_2O_2 faradic efficiency of 70% to 75% was obtained (Supplementary Fig. 26). At an applied cell potential of 0.60 V, the current density remained stable over 100 h, and a relatively high H_2O_2 concentration of 1.08 mol L^{-1} was accumulated, presenting a promising example for the on-site production of H_2O_2 (Fig. 4f).

To gain insight into the role of N_p to the Co−N_4 active site for the ORR, deuterium kinetic isotope effect (KIE) studies were explored. Usually, a KIE > 1 indicates the presence of a proton transfer event involved in the rate-determining step (RDS), whereas a KIE ≈ 1 suggests no proton transfer participation in the RDS. As such, the assessment of KIE is conducive to interpreting the proton transfer kinetics. To evaluate the KIE, we recorded the LSV curves for the ORR in 0.050 M D_2SO_4/D_2O and 0.050 M H_2SO_4/H_2O, respectively. It is important to note that $DClO_4$ is not commercially available, so D_2SO_4 is used instead for KIE experiments. The corresponding H_2O_2 selectivities of Co-N_4 and Co-N_4-N_P in 0.050 M H_2SO_4/H_2O are similar to those in 0.10 M $HClO_4$ (Supplementary Fig. 27), signifying the negligible disturbance of the ORR activity by anions of SO_4^{2-} and ClO_4^- in our case. Moreover, the FE of H_2O_2 formation in the deuterated and normal aqueous electrolytes are similar for each of the catalysts, Co-N_4 and Co-N_4-N_P, ensuring suitable KIE investigations for our system (Supplementary Fig. 28). Figures 5a and 5b show that the LSV curves of Co-N_4 and Co-N_4-N_P collected in deuterated electrolytes exhibit much lower current density than those measured in aqueous electrolytes. The KIE value of Co-N_4-N_P is estimated to be 1.61–1.92 across the potential range of 0.35 V to 0.00 V vs. RHE, implying a rate-determining proton transfer step in the ORR. The comparative Co-N_4 sample presents a more significant primary isotope effect (2.02–2.31) over the applied potential window (Fig. 5c). The smaller value of KIE for Co-N_4-N_P than for Co-N_4 indicates that the existence of a proton transfer relay close to the active center of Co-N_4-N_P facilitates the proton transfer kinetics.

To further prove the possession of proton transfer relay within Co-N_4-N_P for the ORR, electrochemical proton inventory studies were investigated. The proton inventory method is especially effective in identifying the number of exchangeable hydrogenic sites that contribute to the reaction rate. The dependence of reaction rate attenuation on the atom fraction of deuterium of the electrolyte can be

fitted by a modified Kresge-Gross-Butler equation (Eq. (1))[43,44].

$$j_n = j_0(1 - n + n\Phi)Z^n \quad (1)$$

$$n = [D_2O]/([D_2O] + [H_2O]) \quad (2)$$

Where n is the atom fraction of deuterium in the electrolyte (Eq. (2)), j_n is the partial current density for H_2O_2 in the electrolyte at a given n value, j_0 is the partial current density for H_2O_2 in the electrolyte without any D_2O, Φ is the isotopic fractionation factor for the hydrogenic site involved in the rate-determining step (RDS), and Z is a parameter related to the aggregate isotope effect from multiple equivalent hydrogenic sites, called Z-sites.

For Co-N_4, the observed linear attenuation ($Z \approx 1.0$ and $\Phi = 0.46$) suggests a single hydrogenic site (water) is engaged in the RDS of the catalytic process (Fig. 5d, f), aligning with previous findings[43]. In contrast, a non-linear dome-shaped profile with $Z = 1.66$ and $\Phi = 0.37$ is delivered by Co-N_4-N_P. The large Z value revealed that the RDS of O_2 reduction at the active sites of Co-N_4-N_P is coupled with an aggregate inverse-isotope effect from the Z-sites (N_P) (Fig. 5e, f). Additionally, the smaller value of Φ for Co-N_4-N_P reveals that the introduced N_P group offers an extra hydrogenic site that influences the transition-state hydrogen bridges related to proton transfer in the RDS of the ORR. Thus, proton inventory studies strongly corroborate the KIE results, and the introduced N_P group serves as a proton relay, shuttling protons from the bulk solution to the active site and accelerating the protonation kinetics of the ORR.

Mechanism studies

In situ attenuated total reflectance surface-enhanced infrared absorption spectroscopy (ATR-SEIRAS) was applied to identify the ORR intermediates catalyzed by Co-N_4 and Co-N_4-N_P (Supplementary Fig. 29c). Under the O_2-saturated 0.10 M $HClO_4$ electrolyte, a series of ATR-SEIRAS spectra were recorded by varying the potential from 0.80 V to 0.10 V vs. RHE. As shown in Supplementary Fig. 29a, two bands at ~1225 cm^{-1} and 1392 cm^{-1} gradually emerged and increased as the potential decreased stepwise, which are ascribed to the O–O stretching mode of surface-adsorbed *OOH and the OOH bending mode of surface-adsorbed $*H_2O_2$, respectively[36,45]. The latter band, however, was not observed for Co-N_4 under similar conditions, due to its low selectivity toward H_2O_2 (Supplementary Fig. 29b).

Next, density functional theory (DFT) calculations were carried out to shed light on the function of the N_p group and the oxygen reduction mechanism of Co-N_4-N_p (Supplementary Data 1). By far, experimental evidence has shown the successful integration of the N_p group and the exceptional effect on dictating the O_2 reduction pathways. As previously mentioned, the positively polarized carbon atoms around the Co–N_4 site shall be more reactive to the 1,3-dipole. Accordingly, various structures with distinct N_p group locations were exhaustively constructed and calculated using DFT. The corresponding optimized structures and relative stabilities are provided in Supplementary Fig. 30. We observe that the most stable structure bears the N_p group close to the Co–N_4 center. This structure (Figs. 6a and 1c) was thus represented to investigate the ORR process on the Co-N_4-N_p system.

The catalyst activity and selectivity were evaluated in terms of the acidic 4e⁻ and 2e⁻ ORR mechanisms[34,46–49]. As such, we established two criteria: firstly, an ideal catalyst should selectively stabilize the OOH* intermediates with an optimal ΔG(OOH*) close to 4.22 eV to minimize overpotential; secondly, it should destabilize O* species to maximize H_2O_2 selectivity by exposing more top-binding sites. As illustrated in Figure 6b, Co-N_4-N_P demonstrates a lower driving force ($\Delta G(H_2O_2)$-$\Delta G(*O)$) of 0.67 V for H_2O_2 formation compared to Co-N_4 (1.15 V), indicating higher 2e⁻ ORR selectivity for Co-N_4-N_P. Furthermore, the theoretical overpotentials ($\eta_{theoretical}$) for 2e⁻ ORR derived from Co-N_4-N_P are 0.24 V, significantly lower than Co-N_4 (0.57 V), further confirming the favorable 2e⁻ ORR of Co-N_4-N_P. In addition, the calculated theoretical overpotentials as a function OH* bind free energy for our studied catalysts and typical metal catalysts are presented in Fig. 6c. The strong *OH binding is located in the left region, while the weak binding corresponds to the right leg in the volcano plot. Our DFT calculations suggest that the Co-N_4 catalyst has a relatively stronger *OH binding, resulting in the preferred 4e⁻ over the 2e⁻ pathway for the ORR, and therefore, a high selectivity towards water production. Interestingly, the Co-N_4 has a similar limiting potential as Pt implying an excellent 4e⁻ ORR activity, which is in line with the literature[25]. In contrast, the introduction of a pendant amine group around the Co–N_4 site mitigates the OH* binding and consequently shifts the ORR toward the 2e⁻ pathway (very close to the limiting potential 0.7 V), demonstrating a very high activity towards H_2O_2 production. At the same time, Co-N_4-N_p exhibits poor 4e⁻ ORR performance compared to Co-N_4, suggesting an impressive selectivity for H_2O_2. Furthermore, the thermodynamic volcano plots[50] also indicate favorable Co-N_4-N_P kinetics toward H_2O_2 in comparison to Co-N_4 (Supplementary Fig. 31). These results indicate that by positing a pendant amine group in the second sphere of the Co–N_4 site, the selectivity of the ORR process changes dramatically from the H_2O to H_2O_2 production.

To further understand the ORR selectivity of these two systems, we calculated the adsorption energy of *OOH, an indicator of showcasing the ORR proceeded through a 2e⁻ or 4e⁻ pathway (Supplementary Data 1). As shown in Fig. 6d, e, Co-N_4 shows a more prominent electron transfer (0.43 e) from the Co–N_4 center to *OOH than Co-N_4-Np (0.39 e), as Bader analysis determined. The interaction between *OOH and the N_p group via hydrogen bonding, as highlighted in Fig. 6e, further weakens the binding strength of *OOH and makes it ready to desorb as H_2O_2 on the Co-N_4-N_p. On the other hand, the O–O bond of *OOH is slightly longer on Co-N_4 (1.45 Å) than on Co-N_4-N_p (1.42 Å). As a result, the O–O bond of *OOH on Co-N_4 is easier to cleavage, favoring the formation of H_2O. Overall, our calculation results indicate that *OOH binds stronger on Co-N_4 and thus weakens the O–O bond, which makes it ready to break and form H_2O, while *OOH on Co-N_4-N_P has a weaker binding strength and is thus easy to desorb as H_2O_2.

Discussion

In summary, a bio-inspired single-atom catalyst Co-N_4-N_p with a pendant amine group as a second sphere was realized by the 1,3-cycloaddition of an azomethine ylide on the well-documented Co–N_4 single-atom catalyst. The pendant amine group in the second sphere as a proton relay interacts with the adsorbed OOH intermediate and weakens the binding strength of *OOH and makes it ready to desorb as H_2O_2. With the aid of N_p, the shuttle of protons from the bulk solution to the catalytic center becomes favorable, which benefits the protonation of $*O_2$ to *OOH and the subsequent *OOH to *HOOH. As a result, the ORR pathway on Co-N_4 was shifted from a 4e⁻ to a 2e⁻ route by the second sphere, accompanying an increased H_2O_2 selectivity from 28 ± 1.75% to 97 ± 1.13% under acidic conditions. Further proof-of-concept application of Co-N_4-N_P on MEA presents a concrete pure aqueous H_2O_2 production with negligible activity loss over 100 h, holding great potential for on-site applications. Our work elucidated that incorporating the second sphere groups is an effective design principle to regulate the microenvironment and catalytic reactivity of SACs, guiding the rational catalyst design akin to an enzyme.

Methods

Materials

Pyrrole (C_4H_5N, 99%, Bidepharm), Sodium dodecyl sulfate (SDS, 98%, Xilong Scientific), Ammoniumpersulphate (APS, 99%, Xilong Scientific), Ethanol (CH_3CH_2OH, 99%,J&K Scientific), Cobalt(III) acetylacetonate ($Co(acac)_3$, 98%, Bidepharm), Sulfuric acid (H_2SO_4, 98%, Dongguan Dongjiang Chemical Reagent Co., Ltd), N-methyl-2-pyrrolidone (NMP, 98%, Shanghai Macklin Biochemical Technology

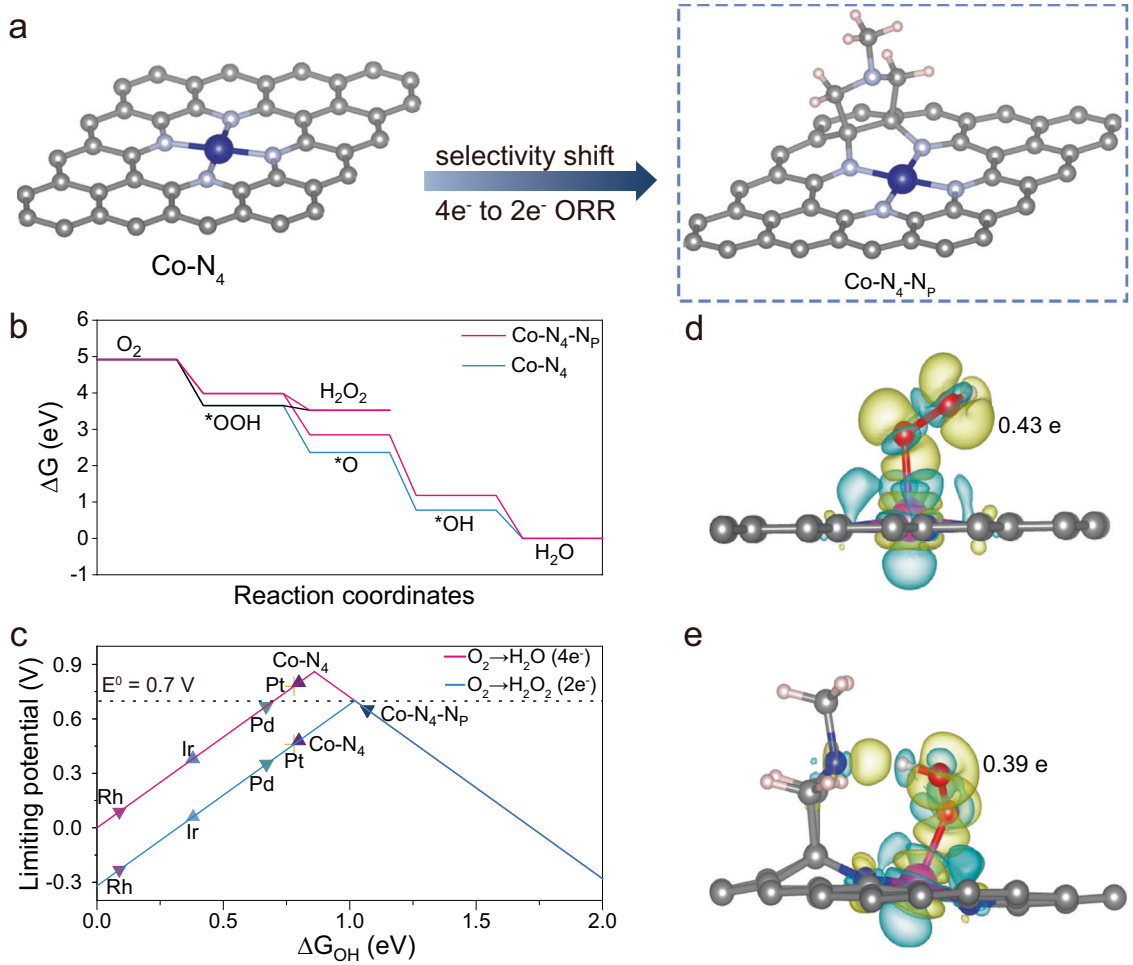

Fig. 6 | ORR mechanism analysis. a The most stable Co-N_4-N_P structure from DFT calculations. **b** Calculated free-energy profiles of the H_2O and H_2O_2 production pathways from oxygen reduction reactions on Co-N_4 and Co-N_4-N_P catalysts. **c** Volcano plot showing the limiting potential of $4e^-$ and $2e^-$ pathways catalyzed by various materials. **d** Differential charge distribution on Co-N_4 with adsorption of *OOH. **e** Differential charge distribution on the Co-N_4-N_P with adsorption of *OOH.

Co., Ltd), Paraformaldehyde ($(CH_2O)_x$, 96%, J&K Scientific), Sarcosine (SAR, 98%, Shanghai Aladdin Biochemical Technology Co., Ltd.) Isopropanol (IPA, 99.5%, Shanghai Macklin Biochemical Technology Co., Ltd), Perchloric acid ($HClO_4$, 72%, Energy Chemical), Commercial PtC (Pt, 20 wt%, Suzhou SineroTechnology Co., Ltd), Silver/Silver Chloride reference electrode (Ag/AgCl, 3 M KCl, Sigma Aldrich Co.), Nafion D-521 Dispersion (5%, Alda Aesar), deuterium oxide (D_2O, 99%, Cambridge Isotope Laboratories,Inc.) were used as received. Millipore water with a resistivity of 18.2 MΩ cm^{-1} was used for all experiments.

Synthesis of Co-N_4

The Co-N_4 was prepared by a soft template strategy. Primary, PPy hydrogels were synthesized by blending 0.30 M pyrrole monomers and 0.10 M SDS in 10 mL deionized water, which was then mixed with 10 mL of 0.30 M ammonium peroxydisulfate aqueous solutions and aged for 2 h. The product was then rinsed with deionized water several times to yield PPy hydrogels. Next, the PPy hydrogels were dispersed in a 40 mL ethanol solution containing 0.0050 M of Cobalt (III) acetylacetonate, $Co(acac)_3$. After stirring for 10 h, the as-obtained Co-PPy hydrogels were rinsed with ethanol and freeze-dried overnight. The product was then transferred to a tube furnace and annealed at 800 °C for 2 h under an Ar atmosphere. As the temperature cooled down to room temperature, the sample was immersed in 2.0 M H_2SO_4 solution for 48 h to leach out any aggregated metal particles or clusters, after which the sample was rinsed with deionized water until the solution pH became neutral. Finally, Co-N_4 was obtained by the second pyrolysis under the above similar conditions. For comparison, the metal-free NC was prepared by direct pyrolysis of PPy hydrogels under the above conditions.

Synthesis of Co-N_4-N_P

The Co-N_4-N_P was synthesized by a 1,3-dipolar cycloaddition reaction. To a two-necked flask, 50 mg of as-prepared Co-N_4 was dispersed in 250 mL N-Methylpyrrolidone, which was then degassed and heated at 160 °C. Then, 89 mg polyformaldehyde and 250 mg sarcosine were added to the above solution with vigorous stirring. After the reaction was completed, the sample was collected and rinsed with deionized water and ethanol several times to deliver the Co-N_4-N_P. The NC-N_P sample was prepared by a similar 1,3-dipolar cycloaddition procedure with NC as the precursor.

Characterizations

The Co content was estimated by the inductively coupled plasma mass spectrometry (Agilent 7700x). XPS was measured on an XSAM800 using Al Kα radiation (1486.6 eV). The adventitious carbon of C 1*s* (284.8 eV) was used as a calibration reference. Co *K*-edge XAS were collected at the BL14W1 beamline of Shanghai Synchrotron Radiation Facility (SSRF) with a Co foil as a calibration reference. C and N *K*-edge XAS were recorded on the soft X-ray beamline at the MCD Endstation of the BL12B-a beamline at the National Synchrotron Radiation Laboratory (NSRL) in Hefei, China. The obtained data were analyzed by Athena and Artemis software. HAADF-STEM was conducted on an FEI

Titan Themis aberration-corrected transmission electron microscopy at 300 kV. TEM and EDX mapping images were carried out on an FEI Talos transmission electron microscope at 200 kV. UV-vis absorption spectra were performed on Agilent Technologies Cary 8454.

Theoretical XANES calculations at the Co K-edge were conducted using the FDMNES code within the real-space full multiple-scattering (FMS) framework, employing the Muffin-tin approximation for the potential[13,51]. The energy-dependent exchange potential was modeled using the Hedin-Lundqvist approach, and the spectra were convoluted with a Lorentzian function whose energy-dependent width accounted for broadening effects from both core-hole interactions and final-state contributions. To ensure the reliability of the calculations, the XANES spectrum for a CoPc reference was computed, demonstrating agreement with experimental results (Supplementary Fig. 8), in line with established findings[13].

Electrochemical tests

The electrochemical ORR measurements were on a CHI 760E workstation with a three-electrode system under an O_2-saturated electrolyte at a room temperature of 25 ± °C. The electrolyte was 0.1 M $HClO_4$ solution (pH = 1.0 ± 0.2)An Ag/AgCl (3.0 M KCl) and a Pt mesh were used as the reference electrode and counter electrode, respectively. The working electrode was the catalysts loaded RRDE (E7R9; Pine instrument company; 0.2475 cm^2 of disc area). To prepare the catalyst ink, 5.0 mg of as-prepared catalyst was dispersed on 975 uL of isopropanol and 25 uL of Nafion solution (5 wt%), followed by sonicated for 1 h. Then, 5 uL of the as-obtained homogeneous dispersion was drop-cast onto the disk electrode of RRDE with a mass loading of 0.20 mg cm^{-2}. The LSV curves were recorded at a scan rate of 10 mV s^{-1} at a rotation speed of 1600 r.p.m. The ring electrode was potentiostat at 1.20 V vs. RHE to quantify the produced H_2O_2. The recorded potentials were converted to the RHE using the equation of:

$$E_{RHE} = E_{Ag/AgCl} + 0.059 \times pH + 0.197 \tag{3}$$

The H_2O_2 selectivity and electron transfer number (n) were calculated based on the following equations:

$$H_2O_2\% = 200^* \frac{I_r/N}{I_d + I_r/N} \tag{4}$$

$$n = 4^* \frac{I_d}{I_d + I_r/N} \tag{5}$$

Where I_r is the ring current, I_d is the disk current, and N is the ring collection efficiency, which was calibrated in 0.050 M $K_3Fe(CN)_6$ and 0.50 M Na_2SO_4 aqueous solutions with different rotation rates. The N was determined as 38%, very close to the theoretical value (Supplementary Fig. 32).

Electrosynthesis of H_2O_2 in MEA

The anode and cathode were the Co-N_4-N_P and commercial 20 wt% Pt/C respective coated gas-diffusion layer (Sigracet 29BC), which then sandwiched a Nafion N117 membrane by a hot press (90 °C and 40 MPa for 5 min) to fabricate an MEA. Nafion N117 membranes (size: 2 cm × 2 cm, typical thickness: 183 μm) were obtained from DuPont de Nemours, Inc. Necessary pretreatment was performed on this membrane prior to its use. The membranes were initially immersed in a hydrogen peroxide solution (H_2O_2, 5 wt%) at 80 °C for 1 h, following which they were washed with Millipore water for a duration of 30 mins. Subsequently, the membranes were boiled once more in a sulfuric acid solution (H_2SO_4, 5 wt%) at 80 °C for 1 h, after which they were rinsed in Millipore water for 30 mins. The MEA was assembled by the two current collectors, which possess serpentine flow channels (2 cm × 2 cm). During electrolysis, the cathode chamber was fed by O_2 and H_2O mixture, and the anode chamber was supplied with humidified H_2 gas. The flow rate of O_2 and H_2 was controlled by a mass flow meter (ALCAT) at a constant flow rate of 80 mL min^{-1} and 50 mL min^{-1}, respectively. The H_2O flow rate was controlled by a peristaltic pump at 2 mL min^{-1}. The concentration of produced H_2O_2 was quantitatively determined by the cerium sulfate $Ce(SO_4)_2$ titration method based on the following formula:

$$2Ce^{4+} + H_2O_2 \rightarrow 2Ce^{3+} + 2H^+ + O_2 \tag{6}$$

The H_2O_2 concentration C_{H2O2} can be calculated as follow:

$$C_{H_2O_2} = 2 \times C_{Ce^{4+}} \tag{7}$$

Where $C_{Ce^{4+}}$ is the mole of reacted Ce^{4+}.

Briefly, 33.2 mg of $Ce(SO_4)_2$ was dispersed in 100 mL of 0.5 M H_2SO_4 as an indicator. The H_2O_2 concentration-absorbance curve was plotted by recording the absorbance values at a wavelength of 320 nm for a series of known H_2O_2 concentrations blended with the above indicator (Supplementary Fig. 33). According to the as-obtained calibration curve, the concentration of the electrochemically produced H_2O_2 can be acquired.

The FE for H_2O_2 production was computed using the following equation:

$$FE = \frac{2 \times C_{H_2O_2} \times F \times \upsilon}{J} * 100\% \tag{8}$$

Where F is the Faraday constant (96485 C mol^{-1}), υ is the water flow rate (L s^{-1}), and J is the measured current (A).

The production rate of H_2O_2 can be calculated as follow:

$$r_{H_2O_2} = 3600 \times C_{H_2O_2} \times \upsilon / A \tag{9}$$

Where A is the area of MEA (4 cm^2).

In situ ATR-SEIRAS measurements

The electrochemical in situ ATR-FTIR measurements were conducted on a Bruker Vertex 80 infrared spectrometer equipped with a liquid nitrogen-cooled detector (LN-MCT Mid). A hemisphere silicon prism (2.5 cm) was sequentially deposited with an Au layer (45 nm) and a Ti layer (3 nm) via an electron beam evaporation system (HHV, TF500). The catalyst ink was then spin-coated onto the hemisphere silicon and assembled in a spectro-electrochemical cell as the working electrode. The counter electrode and reference electrodes were the Pt mesh and Ag/AgCl (3.0 M KCl), respectively. The in situ ATR-SEIRAS spectra were collected at the potential range of 0.80 V to 0.00 V vs. RHE under O_2-saturated 0.1 M $HClO_4$ electrolyte. The spectra were recorded with a resolution of 16 scans per spectrum with a spectral resolution of 4 cm^{-1}. The background infrared spectrum was acquired at the open-circuit potential.

In situ TEM measurements

In situ TEM measurements utilized a Poseidon Select electrochemical cell (Protochips, in situ TEM E-chip cell) to maintain the liquid condition within the microscope. The cell comprised bottom and top E-chips with three electrodes: a glassy carbon working electrode and two Pt electrodes as reference and counter electrodes. Before assembly, the chips underwent methanol and acetone immersion to remove the protective coating, followed by plasma cleaning. Catalyst dispersion in ethanol (5 μL) was drop-casted onto the E-chip, followed by addition of O_2-saturated 0.1 M $HClO_4$ aqueous solution (10 μL) as an electrolyte. Vacuum checking was performed before insertion into the microscope column. Imaging was conducted on a double Cs-aberration-corrected FEI Themis Z G2 microscope (accelerating

voltage: 300 kV). Electrochemical experiments utilized a floating potentiostat (Gamry Reference 600+). Real-time imaging employed chronoamperometry at an applied potential of 0.5 V versus RHE for 40 min. The potential recorded was converted to RHE using:

$$E_{RHE} = E_{Apply} - E_{o-Pt} - 0.059 \times pH \quad (10)$$

$$E_{o-Pt} = -1.18\,V \quad (11)$$

Operando X-ray absorption spectroscopy (XAS) experiments

The operando Co *K*-edge XAS of Co-N_4-N_P was carried out at TPS 32A, National Synchrotron Radiation Research Center (NSRRC), Hsinchu, Taiwan. The photon energy of the incident X-ray was calibrated using Co metal foil as the reference spectrum. All spectra were obtained by measuring the fluorescence using a 7-channel silicon drift detector (SDD). To collect the spectra for in situ experiments, the Co-N_4-N_P was mounted on the working electrode in a customized electrochemical cell, using O_2-saturated 0.1 M $HClO_4$ as the electrolyte with a constant O_2 flow. We applied 0.4 V vs. RHE on the working electrode for 3 h and continuously collected the spectra with a measuring time of 30 minutes for each spectrum. We averaged the resulting spectra hourly and denoted the averaged spectra as 0.4 V for 1 h, 2 h, and 3 h, respectively. The resulting spectra were analyzed using Athena software to obtain the normalized spectra and *r*-space. All spectra were first processed by the typical normalization method. The *r*-space was obtained by the k^3-weighting Fourier transform of the extended X-ray absorption fine structure (EXAFS).

Computational methods

All calculations were carried out using the Vienna Ab Initio Simulation Package (VASP)[52–54] with the BEEF-vdW exchange-correlation functional[55]. An energy cutoff of 450 eV was used and the electronic energy convergence criterion was set to 10^{-5} eV. All structures were relaxed until the Hellmann-Feynman force on each atom were smaller than 0.03 eV $Å^{-1}$. A 15 Å vacuum region has been employed to avoid the periodic slab interactions and dipole correction was applied to the direction perpendicular to the surface. The catalyst was modeled using Co–N_4 motif embedded in a graphene structure with surface cell size of 12.21 Å × 12.21 Å. The Brillouin zone integration is sampled by 4 × 4 × 1 k-points using the Monkhorst-Pack scheme[56]. The theoretical overpotental was calculated as the highest potential where all the reaction steps become downhill in energy for ORR. The free energy correction was obtained by accounting for the zero-point energy (ZPE) and entropic contributions from vibrational degrees of freedom, calculated with the substrate fixed.

Data availability

All data needed to evaluate the conclusions in the paper are present in the paper and/or the Supplementary Information. Source data are provided as a Source data file. Source data are provided with this paper.

References

1. Bullock, R. M. et al. Using nature's blueprint to expand catalysis with earth-abundant metals. *Science* **369**, eabc3183 (2020).
2. Tang, C. et al. Tailoring acidic oxygen reduction selectivity on single-atom catalysts via modification of first and second coordination spheres. *J. Am. Chem. Soc.* **143**, 7819–7827 (2021).
3. Thorseth, M. A., Tornow, C. E., Tse, E. C. M. & Gewirth, A. A. Cu complexes that catalyze the oxygen reduction reaction. *Coord. Chem. Rev.* **257**, 130–139 (2013).
4. Liu, J. et al. Metalloproteins containing cytochrome, iron-sulfur, or copper redox centers. *Chem. Rev.* **114**, 4366–4469 (2014).
5. Solomon, E. I. et al. Copper active sites in biology. *Chem. Rev.* **114**, 3659–3853 (2014).
6. Reek, J. N. H. et al. Transition metal catalysis controlled by hydrogen bonding in the second coordination sphere. *Chem. Rev.* **122**, 12308–12369 (2022).
7. Amanullah, S., Saha, P. & Dey, A. Activating the Fe(I) state of iron porphyrinoid with second-sphere proton transfer residues for selective reduction of CO_2 to HCOOH via Fe(III/II)-cooh intermediate(s). *J. Am. Chem. Soc.* **143**, 13579–13592 (2021).
8. Wang, J., Li, Z., Wu, Y. & Li, Y. Fabrication of single-atom catalysts with precise structure and high metal loading. *Adv. Mater.* **30**, 1801649 (2018).
9. Chen, Y. et al. Single-atom catalysts: Synthetic strategies and electrochemical applications. *Joule* **2**, 1242–1264 (2018).
10. Cui, X., Li, W., Ryabchuk, P., Junge, K. & Beller, M. Bridging homogeneous and heterogeneous catalysis by heterogeneous single-metal-site catalysts. *Nat. Catal.* **1**, 385–397 (2018).
11. Horvath, S., Fernandez, L. E., Soudackov, A. V. & Hammes-Schiffer, S. Insights into proton-coupled electron transfer mechanisms of electrocatalytic H_2 oxidation and production. *Proc. Natl Acad. Sci. USA* **109**, 15663–15668 (2012).
12. Jung, E. et al. Atomic-level tuning of Co-N-C catalyst for high-performance electrochemical H_2O_2 production. *Nat. Mater.* **19**, 436–442 (2020).
13. Fei, H. et al. General synthesis and definitive structural identification of MN_4C_4 single-atom catalysts with tunable electrocatalytic activities. *Nat. Catal.* **1**, 63–72 (2018).
14. Xiao, M. et al. Preferentially engineering FeN_4 edge sites onto graphitic nanosheets for highly active and durable oxygen electrocatalysis in rechargeable Zn-air batteries. *Adv. Mater.* **32**, 2004900 (2020).
15. Li, Q. et al. Fe isolated single atoms on S, N codoped carbon by copolymer pyrolysis strategy for highly efficient oxygen reduction reaction. *Adv. Mater.* **30**, 1800588 (2018).
16. Yang, Y. et al. O-, N-atoms-coordinated Mn cofactors within a graphene framework as bioinspired oxygen reduction reaction electrocatalysts. *Adv. Mater.* **30**, 1801732 (2018).
17. Tang, C. et al. Coordination tunes selectivity: Two-electron oxygen reduction on high-loading molybdenum single-atom catalysts. *Angew. Chem., Int. Ed.* **59**, 9171–9176 (2020).
18. Yuan, K. et al. Boosting oxygen reduction of single iron active sites via geometric and electronic engineering: Nitrogen and phosphorus dual coordination. *J. Am. Chem. Soc.* **142**, 2404–2412 (2020).
19. Qin, R., Liu, K., Wu, Q. & Zheng, N. Surface coordination chemistry of atomically dispersed metal catalysts. *Chem. Rev.* **120**, 11810–11899 (2020).
20. Quintana, M. et al. Functionalization of graphene via 1,3-dipolar cycloaddition. *ACS Nano* **4**, 3527–3533 (2010).
21. Tagmatarchis, N. & Prato, M. Functionalization of carbon nanotubes via 1,3-dipolar cycloadditions. *J. Mater. Chem.* **14**, 437–439 (2004).
22. Ferrandiz-Saperas, M., Ghisolfi, A., Cazorla-Amoros, D., Najera, C. & Sansano, J. M. Multilayer graphene functionalized through thermal 1,3-dipolar cycloadditions with imino esters: A versatile platform for supported ligands in catalysis. *Chem. Commun.* **55**, 7462–7465 (2019).
23. Luo, S.-X. L., Liu, R. Y., Lee, S. & Swager, T. M. Electrocatalytic isoxazoline-nanocarbon metal complexes. *J. Am. Chem. Soc.* **143**, 10441–10453 (2021).
24. Houk, K. N., Sims, J., Watts, C. R. & Luskus, L. J. Origin of reactivity, regioselectivity, and periselectivity in 1,3-dipolar cycloadditions. *J. Am. Chem. Soc.* **95**, 7301–7315 (1973).
25. Jin, Z. et al. Understanding the inter-site distance effect in single-atom catalysts for oxygen electroreduction. *Nat. Catal.* **4**, 615–622 (2021).

26. Girgis, B. S., Temerk, Y. M., Gadelrab, M. M. & Abdullah, I. D. J. C. l. X-ray diffraction patterns of activated carbons prepared under various conditions. *Carbon Lett.* **8**, 95–100 (2007).
27. Ou, B. et al. Covalent functionalization of graphene with poly(-methyl methacrylate) by atom transfer radical polymerization at room temperature. *Poly. Chem.* **3**, 2768–2775 (2012).
28. Han, G.-F. et al. Building and identifying highly active oxygenated groups in carbon materials for oxygen reduction to H_2O_2. *Nat. Commun.* **11**, 2209 (2020).
29. Jeong, H. K. et al. X-ray absorption spectroscopy of graphite oxide. *EPL* **82**, 67004 (2008).
30. Gao, Y. et al. Nitrogen-doped sp^2-hybridized carbon as a superior catalyst for selective oxidation. *Angew. Chem. Int. Ed.* **52**, 2109–2113 (2013).
31. Zhong, J. et al. Probing solid state n-doping in graphene by X-ray absorption near-edge structure spectroscopy. *Carbon* **50**, 335–338 (2012).
32. Zhang, L.-S., Liang, X.-Q., Song, W.-G. & Wu, Z.-Y. Identification of the nitrogen species on N-doped graphene layers and Pt/NG composite catalyst for direct methanol fuel cell. *Phy. Chem. Chem. Phy.* **12**, 12055–12059 (2010).
33. Zhao, Y. et al. Few-layer graphdiyne doped with *sp*-hybridized nitrogen atoms at acetylenic sites for oxygen reduction electrocatalysis. *Nat. Chem.* **10**, 924–931 (2018).
34. Siahrostami, S. et al. Enabling direct H_2O_2 production through rational electrocatalyst design. *Nat. Mater.* **12**, 1137–1143 (2013).
35. Shen, R. et al. High-concentration single atomic pt sites on hollow cusx for selective O_2 reduction to H_2O_2 in acid solution. *Chem* **5**, 2099–2110 (2019).
36. Li, H. et al. Scalable neutral H_2O_2 electrosynthesis by platinum diphosphide nanocrystals by regulating oxygen reduction reaction pathways. *Nat. Commun.* **11**, 3928 (2020).
37. Yang, S., Kim, J., Tak, Y. J., Soon, A. & Lee, H. Single-atom catalyst of platinum supported on titanium nitride for selective electrochemical reactions. *Angew. Chem. Int. Ed.* **55**, 2058–2062 (2016).
38. Zhao, J. et al. Manipulating the oxygen reduction reaction pathway on Pt-coordinated motifs. *Nat. Commun.* **13**, 685 (2022).
39. Verdaguer-Casadevall, A. et al. Trends in the electrochemical synthesis of H_2O_2: Enhancing activity and selectivity by electrocatalytic site engineering. *Nano Lett.* **14**, 1603–1608 (2014).
40. Zhang, E. et al. Engineering the local atomic environments of indium single-atom catalysts for efficient electrochemical production of hydrogen peroxide. *Angew. Chem. Int. Ed.* **61**, e202117347 (2022).
41. Wan, J. et al. In situ phosphatizing of triphenylphosphine encapsulated within metal-organic frameworks to design atomic Co_1-P_1N_3 interfacial structure for promoting catalytic performance. *J. Am. Chem. Soc.* **142**, 8431–8439 (2020).
42. Chen, Y. et al. Atomic-level modulation of electronic density at cobalt single-atom sites derived from metal-organic frameworks: Enhanced oxygen reduction performance. *Angew. Chem. Int. Ed.* **60**, 3212–3221 (2021).
43. Li, W. et al. A bio-inspired coordination polymer as outstanding water oxidation catalyst via second coordination sphere engineering. *Nat. Commun.* **10**, 5074 (2019).
44. Liu, Y. & McCrory, C. C. L. Modulating the mechanism of electrocatalytic CO_2 reduction by cobalt phthalocyanine through polymer coordination and encapsulation. *Nat. Commun.* **10**, 1683 (2019).
45. Nayak, S., McPherson, I. J. & Vincent, K. A. Adsorbed intermediates in oxygen reduction on platinum nanoparticles observed by in situ IR spectroscopy. *Angew. Chem. Int. Ed.* **57**, 12855–12858 (2018).
46. Kulkarni, A., Siahrostami, S., Patel, A. & Nørskov, J. K. Understanding catalytic activity trends in the oxygen reduction reaction. *Chem. Rev.* **118**, 2302–2312 (2018).
47. Nørskov, J. K. et al. Origin of the overpotential for oxygen reduction at a fuel-cell cathode. *J. Phys. Chem. B* **108**, 17886–17892 (2004).
48. Viswanathan, V., Hansen, H. A., Rossmeisl, J. & Nørskov, J. K. Universality in oxygen reduction electrocatalysis on metal surfaces. *ACS Catal.* **2**, 1654–1660 (2012).
49. Zhong, L. & Li, S. Unconventional oxygen reduction reaction mechanism and scaling relation on single-atom catalysts. *ACS Catal.* **10**, 4313–4318 (2020).
50. Exner, K. S. Steering selectivity in the four-electron and two-electron oxygen reduction reactions: On the Importance of the volcano slope. *ACS Phys. Chem. Au* **3**, 190–198 (2023).
51. Joly, Y. X-Ray absorption near-edge structure calculations beyond the muffin-tin approximation. *Phys. Rev. B* **63**, 125120 (2001).
52. Kresse, G. & Hafner, J. Ab initio molecular dynamics for liquid metals. *Phys. Rev. B Condens. Matter* **47**, 558–561 (1993).
53. Kresse, G. & Furthmüller, J. Efficiency of ab-initio total energy calculations for metals and semiconductors using a plane-wave basis set. *Comput. Mater. Sci.* **6**, 15–50 (1996).
54. Kresse, G. & Joubert, D. From ultrasoft pseudopotentials to the projector augmented-wave method. *Phys. Rev. B* **59**, 1758–1775 (1999).
55. Wellendorff, J. et al. Density functionals for surface science: Exchange-correlation model development with bayesian error estimation. *Phys. Rev. B* **85**, 235149 (2012).
56. Monkhorst, H. J. & Pack, J. D. Special points for Brillouin-zone integrations. *Phys. Rev. B* **13**, 5188–5192 (1976).

Acknowledgements

This work is supported by the National Natural Science Foundation of China (22179057, L.D., 42050203, H.D.,), the Stable Support Plan Program of Shenzhen Natural Science Fund (20200925152742003), and the Educational Commission of Guangdong Province (2020KTSCX121). We acknowledge the support from the BL11B station at Shanghai Synchrotron Radiation Facility (SSRF). We thank H.C., and Y.C., at TPS 32A, National Synchrotron Radiation Research Center (NSRRC), Hsinchu, Taiwan for their technical support on Operando XAS experiments.

Author contributions

L.D., supervised the project. H.Z., and S.S., conducted the experiments. H.D., and W.L., conducted XAS experiments. L.D., H.Z., W.Y., and Z.W., wrote the paper. W.Y., and Z.W., performed the DFT calculations. M.C., H.L., F.L., and J.H., help in the FTIR analysis. H.C., and Y.C., performed operando XAS measurement. All authors discussed the results and assisted in the manuscript preparation.

Competing interests

The authors declare no competing interests.

Additional information

Supplementary information The online version contains supplementary material available at https://doi.org/10.1038/s41467-024-55116-x.

Correspondence and requests for materials should be addressed to Lele Duan.

Peer review information *Nature Communications* thanks Kai Exner, and the other, anonymous, reviewer(s) for their contribution to the peer review of this work. A peer review file is available.